

# Diffraction Alvarez-Lohmann lenses for correcting aberrations of tunable membrane lenses

Leonhard Lenk<sup>✉\*</sup> and Stefan Sinzinger<sup>✉</sup>

Technische Universität Ilmenau, Institut für Mikro und Nanotechnologien IMN MacroNano,  
Fakultät für Maschinenbau, Technische Optik, Ilmenau, Germany

**Abstract.** Focus-tunable lenses, e.g., liquid filled membrane lenses (MLs), have found increasingly widespread application in optical systems. If a large refractive power range is to be used, the correction of chromatic aberrations is particularly challenging: a group containing a single ML cannot be corrected over the whole refractive power range. In analogy to hybrid achromats for lenses with constant focal lengths, we present the combination of an ML and a diffractive Alvarez-Lohmann-lens (ALL) for the compensation of axial color over a large refractive power range. In contrast to the combination of multiple MLs, this does not increase the axial length of the system significantly. At the same time, the flexible adaption of the phase function of the diffractive ALL can reduce spherical aberration over the whole focal range. Design examples with ray-tracing and wave-optical simulations demonstrate the performance of the resulting hybrid tunable element. Experimental data from fabricated sample lenses provide a proof of principle. © The Authors. Published by SPIE under a Creative Commons Attribution 4.0 International License. Distribution or reproduction of this work in whole or in part requires full attribution of the original publication, including its DOI. [DOI: [10.1117/1.OE.62.3.035103](https://doi.org/10.1117/1.OE.62.3.035103)]

**Keywords:** adaptive optics; liquid lens; diffractive optics; membrane lens; Alvarez; Lohmann.

Paper 20221380G received Nov. 22, 2022; accepted for publication Feb. 22, 2023; published online Mar. 19, 2023.

## 1 Introduction

Tunable lenses, which are able to change their focal length without axial motion of the optical elements, are based on a wide range of technologies.<sup>1-3</sup> One of the most widespread concepts for refractive tunable lenses is changing the curvature of a surface. This surface can be a liquid filled membrane [membrane lens (ML<sup>4-6</sup>)] or the interface of two non-mixing liquids (fluidic lens<sup>7,8</sup>). Promising applications are focusing lenses or even zoom systems, in which the tunable lenses can replace the axial motion of lens groups, which seems especially advantageous for compact lens modules.

The design of such systems is challenging: color correction over the whole tuning range for groups with a single tunable lens is difficult and compensating for the strong variation in the surface contributions to other aberrations is not easy. A tunable counterpart to the well-known achromatic doublet that can be employed within those more complex optical systems or used alone for applications with lower requirements is therefore desirable. In analogy to classical achromats, a possible solution is the combination of tunable lenses employing liquids with crown- and flint-like behavior, respectively (e.g., Ref. 9). Unfortunately, this comes at the cost of an increased system length and reduces the tuning ranges of the corrected groups due to the necessity of a positive-negative combination of refractive powers.<sup>10,11</sup>

Here the well-known concept of hybrid refractive-diffractive achromats offers a promising alternative. A tunable variation of these achromats can be implemented by combining the refractive tunable lens with a so-called diffractive Alvarez-Lohmann lens (ALL). These lenses consist of two diffractive phase elements that change the resulting focal length by being translated or rotated relative to each other and perpendicular to the optical axis.<sup>12-18</sup> Although this requires installation space for precise motion of the optical elements, typical miniaturized applications usually offer at least one direction perpendicularly to the optical axis, where installation space is less critical. This is particularly true for smartphone camera lenses, where the thickness of the

\*Address all correspondence to Leonhard Lenk, [leonhard.lenk@tu-ilmenau.de](mailto:leonhard.lenk@tu-ilmenau.de)

device usually forms the most critical dimension and installation space in other directions is slightly more relaxed. In general, the option of distributing installation space between the axial direction and other dimensions offers increased flexibility. Furthermore, due to the negative Abbe number of diffractive lenses, the sign of the diffractive ALL's refractive power is the same as the refractive power of the refractive tunable lens. This even increases the tuning range of the corrected lens group, compared with the tuning range of the refractive tunable lens itself.

Additionally, various authors have demonstrated the application of ALLs for influencing monochromatic aberrations; e.g., Bielke et al.<sup>19</sup> used diffractive ALLs for compensation of astigmatism in interferometry. Grewe et al. showed the application of higher polynomial terms in refractive ALLs for correction of aberrations in imaging systems<sup>20</sup> and in diffractive ALLs for confocal hyperspectral systems.<sup>21</sup> Similar to that, the use of higher polynomial terms for the phase function of the ALL can partially compensate for the spherical aberration of the refractive tunable lens over the whole tuning range. Thereby, the performance of a combination of one refractive lens with one ALL can conceptually come close to the performance of a real tunable achromat.

Similar approaches exist and include the combination of diffractive liquid-crystal lenses for color correction of MLs, without addressing spherical aberration<sup>22</sup> and even the combination of a rotational, diffractive ALL with a ML but with the slightly different objective of keeping a constant focal length while independently tuning the axial color.<sup>23</sup>

We demonstrate the potential of the proposed hybrid element based on two design examples, using ray-tracing and wave-optical simulations as well as experimental evaluations of fabricated diffractive ALLs for the correction of a commercial ML.<sup>24</sup>

## 2 Basic Principle

### 2.1 Alvarez-Lohmann Lenses

In general, ALLs are based on using the sum of the phase functions of two elements, which are directly placed behind each other. By displacing the two phase elements, the resulting phase function can be varied continuously (Fig. 1). The phase elements can be refractive or diffractive optical elements.<sup>12,13</sup>

For the diffractive variation of the ALLs, displacement of the phase elements can be translational or rotational. The rotational diffractive ALLs are also referred to as diffractive Moiré

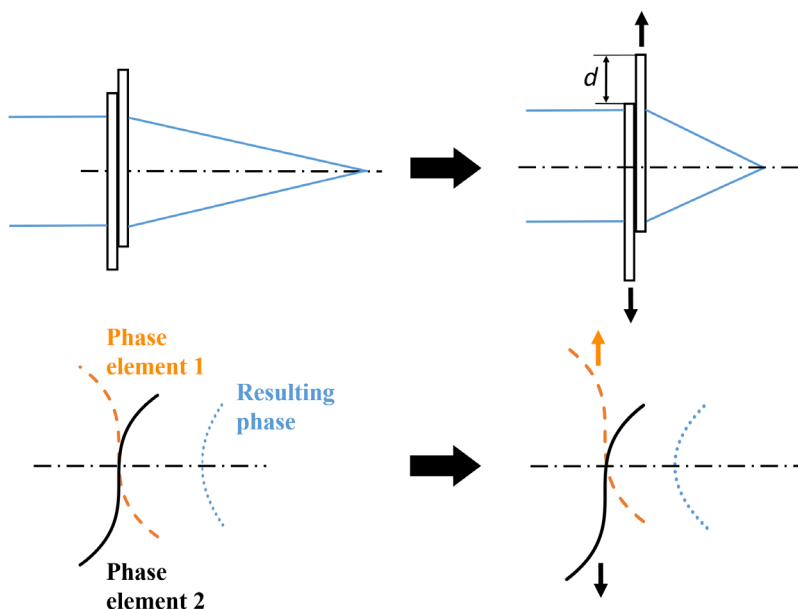


**Fig. 1** Principle of translational diffractive Alvarez-Lohmann lenses (ALLs) with element shift  $d$ .

**Table 1** Equations for phase functions of rotational and translational diffractive ALLs. <sup>12-14</sup>

<b>Rotational diffractive ALLs (Moiré lenses)</b> <sup>14</sup>	
Phase element 1	$\Phi_{\text{rot},1}(r, \varphi) = \text{round}(Ar^2)\varphi$
Phase element 2	$\Phi_{\text{rot},2}(r, \varphi) = -\text{round}(Ar^2)\varphi$
Resulting phase	Sector I: $\Phi_{\text{rotI}} = \text{round}(Ar^2)(\Theta - 2\pi)$ , Sector II: $\Phi_{\text{rotII}} = \text{round}(Ar^2)\Theta$ (rounding to full integers, for avoidance of sectors with parasitic focal lengths)
Minimum period of diffractive structure	$p_{\text{rot,min}} = \frac{1}{AR}$
Absolute maximum refractive power	$F'_{\text{rot,m}} = \frac{A\lambda_0\Theta_{\text{max}}}{\pi}$
<b>Translational diffractive ALLs (shift in the x-direction)</b> <sup>12,13</sup>	
Phase element 1	$\Phi_{\text{trans},1}(x, y) = A\left(\frac{1}{3}x^3 + xy^2\right)$
Phase element 2	$\Phi_{\text{trans},2}(x, y) = -A\left(\frac{1}{3}x^3 + xy^2\right)$
Resulting phase	$\Phi_{\text{trans}}(x, y, d) = -2Ad(x^2 + y^2) - \frac{2}{3}Ad^3$
Minimum period of diffractive structure, circular aperture ( <a href="#">Appendix A</a> )	$p_{\text{trans,min}} = \frac{2\pi}{A(R+d_{\text{max}})^2}$
Absolute maximum refractive power	$F'_{\text{trans,max}} = \frac{2A\lambda_0 d_{\text{max}}}{\pi}$
Symbols	<p><math>r</math>, radial coordinate;</p> <p><math>\Phi</math>, angular coordinate;</p> <p><math>A</math>, coefficient for slope of tuning function;</p> <p><math>\Theta</math> angle of relative element rotation;</p> <p><math>R</math>, radius of aperture;</p> <p><math>\lambda_0</math> designwavelength; and</p> <p><math>d</math>, absolute element shift relative to optical axis.</p>

lenses. <sup>14-17</sup> Table 1 shows the equations for the phase functions of the translational and rotational diffractive ALLs, as well as the resulting parabolic phase function and the equations for the minimum period of the diffractive structures.

An important factor for the fabrication of the diffractive optical elements is the minimum feature size, determined by dividing the minimum period of the diffractive structures ([Appendix A](#)) by the number of phase levels. For a given tuning range and aperture diameter of the ALL, this minimum period can be influenced by changing the steepness of the tuning function  $A$ . This is done by determining the maximum shift or angle of rotation, respectively, which is necessary to reach the limits of the tuning range for translationally or rotationally tuned ALLs.

For rotational diffractive ALLs, the maximum angle of rotation that is recommended is  $0.5\pi$ , to keep the maximum diffraction efficiency above 85%, as described in Ref. 14. There is no comparable limit for the maximum shift in translationally tuned ALLs; usually the most important limit is the available installation space.

Figure 2(a) shows the comparison of the minimum period of the diffractive structures for rotational ALLs for the maximum angle of rotation and different maximum shifts for the translational diffractive ALLs. The quantities used in the comparison are in the range of the requirements for an ALL used to correct an exemplary ML with a tuning range of about  $-18$  to  $+18$  dpt.

It clearly shows that, for the considered tuning range and aperture diameter, there is a wide range of reasonable maximum shift values that allow the translational ALLs to work with larger minimum periods of the diffractive structures than the rotationally tuned ALL. Following

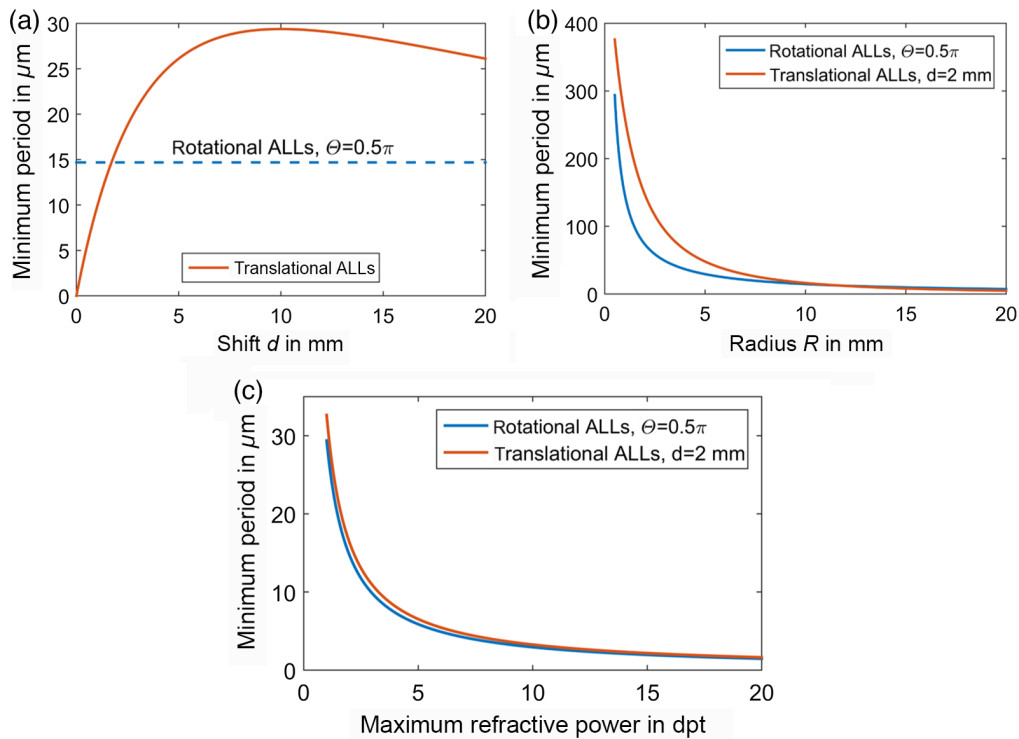


**Fig. 2** Comparison of minimum periods of diffractive structures for parabolic translational and rotational ALLs with a maximum refractive power of 2 dpt at a design wavelength of 587.562 nm ( $d$ -line) and with the maximum recommended rotation of the rotational ALLs of  $\Theta = 0.5\pi$ . (a) At a constant aperture radius of 10 mm, (b) for a constant shift of 2 mm, and (c) for a constant aperture radius of 10 mm and a constant maximum shift of 2 mm and different tuning ranges (defined by the maximum refractive power).

Fig. 2(b), for an exemplary maximum shift value of 2 mm, this advantage is larger for smaller aperture diameters and disappears when a certain aperture diameter is reached. Figure 2(c) demonstrates that a larger tuning range, given by the maximum refractive power, only very slowly reduces the advantage of the translationally tuned ALLs. The larger minimum periods alleviate fabrication constraints, which e.g., define minimum feature sizes. For the mask-based lithographic processes, employed in following sections, this minimum feature size is at about 1  $\mu\text{m}$  (Sec. 5.1).

Furthermore, the rotational ALLs require an additional radial quantization step to avoid the formation of sectors with parasitic focal lengths (Table 1), which still leads to a bifocal behavior that splits the diffraction efficiency between the two foci depending on the angle of rotation.<sup>14</sup> A major drawback of the translational ALLs over the rotationally tuned type is the requirement to precisely move the two elements symmetrically in opposite directions, which complicates the mechanical setup. This is known from refractive ALLs, and the corresponding literature provides multiple approaches to address this challenge, including mechanical systems that only require one single actuator for both elements.<sup>25</sup> Another remaining advantage of the rotational ALLs is that they do not require additional installation space for moving, which is especially interesting for miniaturized applications. However, because typical applications of highly integrated systems provide one direction perpendicular to the optical axis where installation space is not too critical and quite small amounts of shift should be enough for the presented application, further considerations focus on the translational ALLs.

## 2.2 Toward “Hybrid Tunable Achromats”

An achromat is generally corrected for the axial color for two wavelengths and at the same time is corrected for spherical aberration. It is well known that the small, negative Abbe number of

diffractive lenses ( $\nu_{d,\text{diff}} = -3.45^{26}$ ) can be used for the correction of the axial color caused by refractive lenses.

Because the Abbe number of the diffractive lenses has a small absolute value, a small refractive power of the diffractive element is enough to compensate for the axial color of a refractive lens with a much larger refractive power. Therefore, a diffractive tunable lens only requires a much smaller tuning range than the refractive tunable lens that is to be corrected.

As a consequence of the negative sign of the Abbe number of diffractive lenses, the sign of the refractive power of the diffractive lens can be the same as the refractive power of the corrected refractive lens. The resulting tuning range of the corrected hybrid lens is thus larger than the tuning range of the uncorrected tunable lens. This is the most important difference to the combination of two refractive tunable lenses with different materials, in which the refractive powers must have opposite signs and thereby reduce the tuning range of the resulting corrected element.<sup>10,11</sup> For a numerical comparison of the achievable performance, we assume two optical liquids for commercial MLs with a comparatively large difference in Abbe numbers: OL1224 with  $\nu_{d,\text{crown}} = 108.49$  and OL0901 with  $\nu_{d,\text{flint}} = 30.276$  (materials taken from the Optotune Zemax<sup>®</sup> model<sup>27</sup>). It is well known that, for the correction of the axial color of two wavelengths, the relation between the refractive powers ( $F'_1, F'_2$ ) and the Abbe numbers within a doublet must satisfy the following condition:<sup>28</sup>

$$\frac{F'_1}{\nu_1} + \frac{F'_2}{\nu_2} = 0. \quad (1)$$

Assuming thin elements and a distance of zero between the elements, the maximum refractive power of the corrected doublet is

$$F' = F'_1 \cdot \left(1 - \frac{\nu_2}{\nu_1}\right). \quad (2)$$

For an ML with a refractive power tuning range of  $-20$  to  $20$  dpt ( $\Delta F'_{\text{ML}} = 40$  dpt), this results in a corrected tuning range of  $\Delta F'_{\text{ref,doublet}} = 28.84$  dpt for the refractive doublet and  $\Delta F'_{\text{diff,doublet}} = 41.27$  dpt for the hybrid doublet, which is quite a substantial difference.

For the compensation of spherical aberration, it is possible to introduce additional phase terms to the phase functions of the ALL elements to influence the asphericity of the originally parabolic shape of the resulting phase function. Busch et al showed in Ref. 29 that the relation between the phase function of a single ALL element can be approximated quite well by the integral of the resulting phase function of the whole ALL. With that in mind, the use of higher polynomial terms for the phase functions of the single ALL elements can be understood as a Taylor approximation of the integral of the desired aspheric phase. Because the aspherical phase function of the diffractive ALL is also affected by the strong diffractive chromatic aberration, this compensation of spherical aberration is limited. Therefore, the hybrid element will generally not reach the full performance of a real achromat.

At this point, it must be noted that, for the refractive tunable doublet with only two membranes, the correction of spherical aberration also requires very specific material parameters, analogous to a cemented doublet for fixed focal length lenses<sup>28</sup> (actually three membranes are needed to reach the degrees of freedom of a cemented fixed focal length doublet over the full tuning range). So this is not necessarily a clear disadvantage of the hybrid tunable doublet compared with the refractive one.

### 3 Design Examples

#### 3.1 Predesign

To demonstrate the possibilities and performance of the hybrid tunable doublets, two ALLs are designed to correct the commercial ML “ML-20-37-VIS-36D-C” from Optotune.<sup>27</sup> The most important characteristics of the ML are shown in Table 2.

**Table 2** Selected characteristics of Optotune ML-20-37-VIS-36D-C, data from official Optotune Zemax<sup>®</sup> model, and ML-20-37 datasheet.<sup>27</sup>

ML-20-37-VIS-36D-C	
Tuning range	−19.6 to 15.6 dpt
Tuning range based on back focal length	18 to 18 dpt
Aperture diameter (recommended)	16 mm
Full aperture diameter	20 mm
Refractive index	$n_d = 1.3823$
Abbe number	$\nu_d = 64.8$

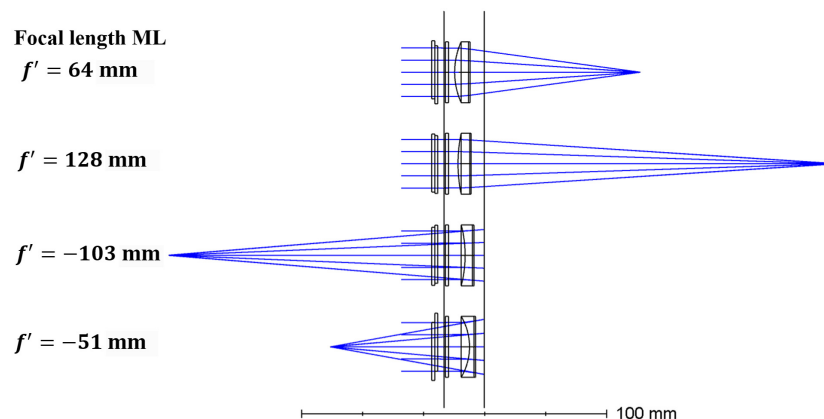
From Eq. (2) the necessary tuning range of the ALLs for the axial color correction results in  $-1.04$  to  $0.828$  dpt. From this and a first, arbitrary maximum shift of  $1$  mm, the coefficient  $A$  for the basic, parabolic ALL phase is computed to be  $2.78 \frac{1}{\text{mm}^3}$ , and is used as the starting point for optimization in Zemax<sup>®</sup> for both designs. The individual diffractive elements are modeled as ideal phase elements by Binary 1 surfaces in Zemax<sup>®</sup>.

Like typical non-tunable achromatic doublets, the hybrid elements are optimized for imaging on the axis for an object at infinity. The wavelengths used are  $486.133$  nm ( $F$ -line),  $587.562$  nm ( $d$ -line), and  $656.273$  nm ( $C$ -line).

### 3.2 Design 1

In the first design, the ALL is placed in front of the ML, and the whole recommended aperture diameter of the ML of  $16$  mm is used (Fig. 3). To leave space for mounting the ALL, the distance between ALL and the housing of the ML is set to  $2$  mm. The ALL elements are placed directly behind each other with a distance of zero. As a first step, the coefficient  $A$  for the basic parabolic phase is optimized for a maximum shift of  $1$  mm for a minimum spot radius. This leads to a small deviation from the theoretical maximum absolute refractive power determined for correction of the axial color. The next step is the selection of the maximum shift, based on the new maximum absolute refractive power of  $1.44$  dpt for the  $d$ -line (Fig. 4).

With a desired number of eight phase levels in the final element and a minimum feature size, which is defined by the manufacturing capabilities at  $1 \mu\text{m}$ , the minimum acceptable period is  $8 \mu\text{m}$ . However, for the sake of sensitivity to fabrication tolerances, as well as alignment tolerances, it is desirable to choose the minimum period of the diffractive structures to be as large as possible. Even without fixed installation space requirements, the maximum shift should be as small as possible for demonstration purposes. For the same reason, we want to stay within the region where the translational ALL offers larger minimum periods than the rotational ALL. With

**Fig. 3** Layout of design 1; the vertical black lines denote the housing of the ML.

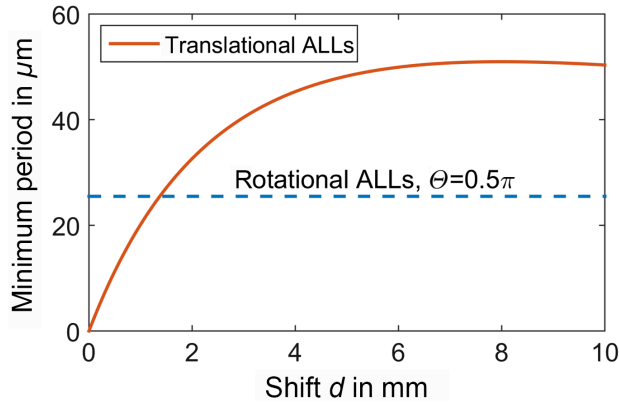


**Fig. 4** Minimum period of diffractive structures versus shift for design 1 at a maximum absolute refractive power of 1.44 dpt at a design wavelength of 587.562 nm ( $d$ -line) and an aperture diameter of 16 mm.

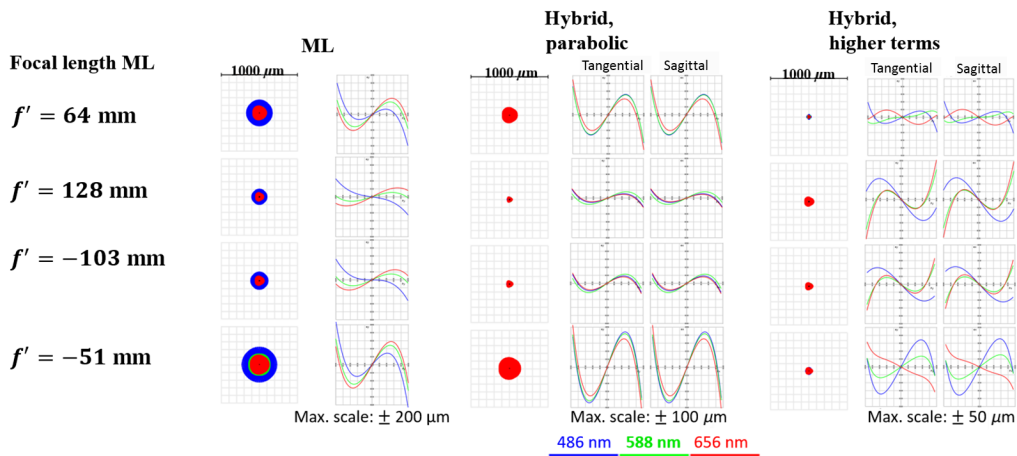
this, the maximum absolute shift is chosen to be 1.5 mm. The minimum period of the diffractive structures results in about  $27 \mu\text{m}$ , which means a minimum feature size of about  $3.375 \mu\text{m}$  for an implementation with eight phase levels. For the subsequent optimization with higher phase terms, a self-written macro is used to limit this minimum feature size to at least  $3 \mu\text{m}$  within the merit function in Zemax<sup>®</sup>, so the period is kept above  $24 \mu\text{m}$ .

Figure 5 shows the results of the optimization compared with the ML alone.

The ray aberration plots in Fig. 5 clearly show that the parabolic ALL improves the axial color. The remaining aberrations are clearly dominated by spherical aberration, which can be seen from the distinctive “s-shape” of the transverse ray aberration curves. For the hybrid element using an ALL with higher phase terms, spherical aberration is clearly reduced. As expected, this comes at the cost of increased differences between the behaviors of the different wavelengths. Figure 6 shows the phase function of one ALL element, with the minimum structure period being about  $25 \mu\text{m}$  (about  $3.1 \mu\text{m}$  minimum feature size for an eight phase level implementation). Table 3 summarizes the relative shifts of the ALL elements for final design 1 with higher phase terms, and the full surface data of design 1 can be found in Appendix B.

### 3.3 Design 2

In design 2, the ALL is placed behind the ML (Fig. 7). Due to mechanical restrictions caused by the ML’s  $C$ -mount adapter, the maximum diameter of the ALL for a distance of 2 mm to the ML



**Fig. 5** Comparison of spot diagrams and transversal ray aberrations for ML alone, hybrid element of ML and ALL with purely parabolic phase, and the hybrid element consisting of ML and ALL with higher phase terms for design 1. Please note the different scaling of the ray aberration plots.

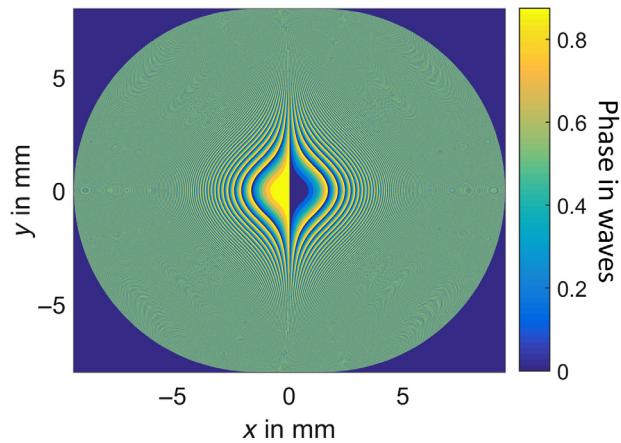


**Fig. 6** Phase function of one ALL element of design 1 with eight phase levels.

**Table 3** Shift values for the ALL in final design 1.

Focal length ML in mm	64	128	-103	-51
Shift d in mm	0.82	0.237	-0.341	-1.5

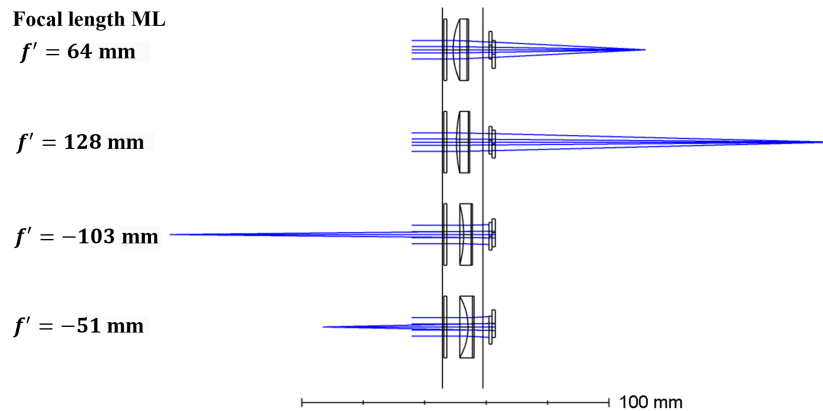


**Fig. 7** Layout of design 2; the vertical black lines denote the housing of the ML.

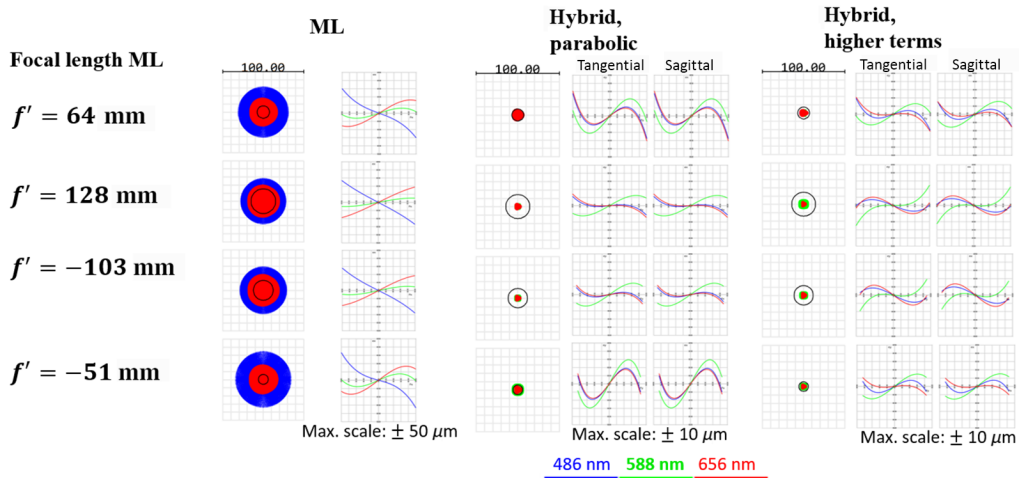
housing is limited to about 6 mm. The distance between the ALL elements is zero. The steps during design are the same as for design 1. The results can be seen in Fig. 8.

Figure 8 shows the same behavior for design 2 as for design 1, although in design 2, the improvement achieved by the higher phase terms is much smaller due to the small contributions of spherical aberration caused by the small aperture. Figure 9 shows the phase function of one ALL element, with the minimum structure period being 148  $\mu\text{m}$  (about 18.5  $\mu\text{m}$  minimum feature size for an 8 phase level implementation). The relative shifts for the different focal lengths are shown in Table 4, and the surface data of design 2 can be found in Appendix C.

## 4 Wave-Optical Simulation

### 4.1 Motivation

The ray-tracing simulations in Zemax<sup>®</sup> treat the diffractive phase elements of the ALLs as ideal phase elements, which always add a certain phase value to an incoming ray. However, even in the scalar approximation in wave optics, which will be used in the following, the effective phase



**Fig. 8** Comparison of spot diagrams and transversal ray aberrations for ML alone, hybrid element of ML and ALL with purely parabolic phase, and the hybrid element consisting of ML and ALL with higher phase terms for design 2. Please note the different scaling of the ray aberration plots.

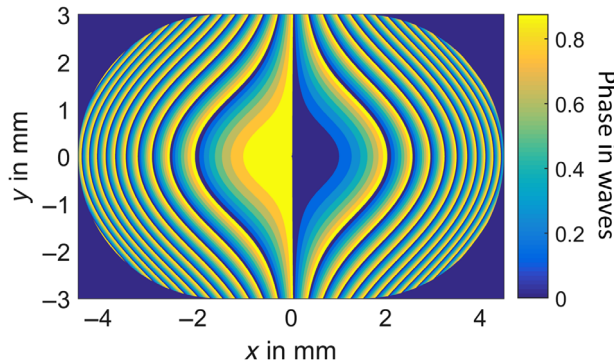


**Fig. 9** Phase function of one ALL element of design 2 with eight phase levels.

**Table 4** Shift values for the ALL in final design 2.

Focal length ML in mm	64	128	-103	-51
Shift <i>d</i> in mm	1.5	0.606	-0.564	-1.062

function is strongly wavelength dependent. Equation (3) gives the effective phase function for a general wavelength of a diffractive optical element in air as<sup>30</sup>

$$\Phi(\lambda) = \frac{\lambda_0 n(\lambda) - 1}{\lambda n(\lambda_0) - 1} \Phi(\lambda_0). \tag{3}$$

Additionally, the real diffractive elements are not fabricated with analogous profiles but are quantized with a limited number of phase levels. In the present case, the number of phase levels is 8. Both quantization and wavelength dependence cause the ratio of incoming intensity at the diffractive element to the intensity within the desired diffraction order, which is called diffraction efficiency, to be smaller than one. To estimate the impact of the diffraction efficiency on the presented designs, a wave-optical simulation is performed.

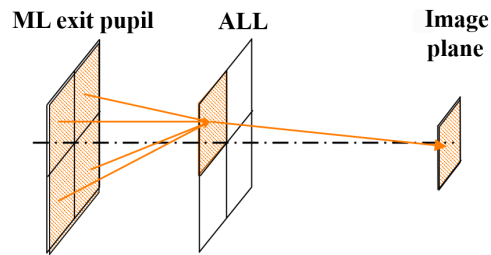


**Fig.10** Principle of wave-optical simulation using subapertures for reduced memory requirements.

## 4.2 Approach

For the wave-optical simulation, the scalar approximation is used, and the ALL is approximated as a thin element. The ML is represented by the aberrated wavefront in its exit pupil, which is exported from Zemax<sup>®</sup> using Zernike standard coefficients, similar to the creation of custom made black-box systems in Zemax<sup>®</sup> as described in Ref. 31. This wavefront is propagated into the plane of the ALL, and the phase functions of both elements of the ALL are added to the propagated wave (Fig. 10). The resulting wavefront is then propagated to the image plane. Because this only works for a hybrid element with the ALL behind the ML, design 2 is used for the estimation of the impact of diffraction efficiency.

The applied propagation algorithm is the shifted band limited angular spectrum method.<sup>32</sup> It allows for efficient scalar propagation by laterally shifting the target window relative to the source window, and it is not limited to the paraxial region. To further reduce the computational load, especially regarding memory requirements, for reasonable apertures at high sampling rates, the planes of the ML's exit pupil and the ALL are split into subapertures (Fig. 10). Propagation is performed separately for each subaperture, and the complex amplitudes of the propagated waves are summed to determine the wavefront within the target subaperture. Because the most interesting part of the image plane for on axis imaging is close to the optical axis, the image plane is only represented by one subaperture. This approach allows for performing the simulation with only the memory load of one subaperture instead of the full aperture. However, because the sampling in frequency space is the reciprocal of the maximum size of the subaperture, the subapertures must not get too small. Therefore, the wave-optical simulations for the considered minimum focal lengths are limited to an aperture diameter of 4 mm on a system with 8-GB RAM.

Propagation is performed separately for each wavelength (*F*-line, *d*-line, and *C*-line), always using the effective phase function for the ALL elements according to Eq. (3).

The resulting intensities in the image plane are the incoherent, monochromatic point spread functions (PSFs). The incoherent, polychromatic PSF is calculated as the sum of the monochromatic PSFs. The Fourier transformed PSFs, computed by fast Fourier transformation, yield the monochromatic and polychromatic modulation transfer functions (MTFs), respectively.<sup>33</sup> These are normalized to their maximum value for evaluation. The whole wave-optical simulation is implemented and performed in Matlab<sup>®</sup>.

## 4.3 Results

Figure 11 shows the MTF data resulting from wave-optical simulation of design 2 with a reduced aperture diameter of 4 mm. The design wavelength of the diffractive elements is at the *d*-line (587.562 nm), and they are quantized to eight phase levels. The aperture is divided into four subapertures. The minimum sampling requirement for each subaperture is estimated beforehand to be  $3514 \times 3514$  using the Nyquist criterion for a Fresnel lens with a slightly shorter focal length than the ML (62 mm) and an oversampling factor of 2. Therefore, each subaperture is sampled by  $3600 \times 3600$  pixels (pixel size:  $0.56 \mu\text{m}$ ); additionally it is zero-padded to twice its size in each dimension (i.e., to four times its area).

The data in Fig. 11(a) show that, even when diffraction efficiency effects are considered, the hybrid element still can be expected to perform better than the ML alone, apart from a drop of the

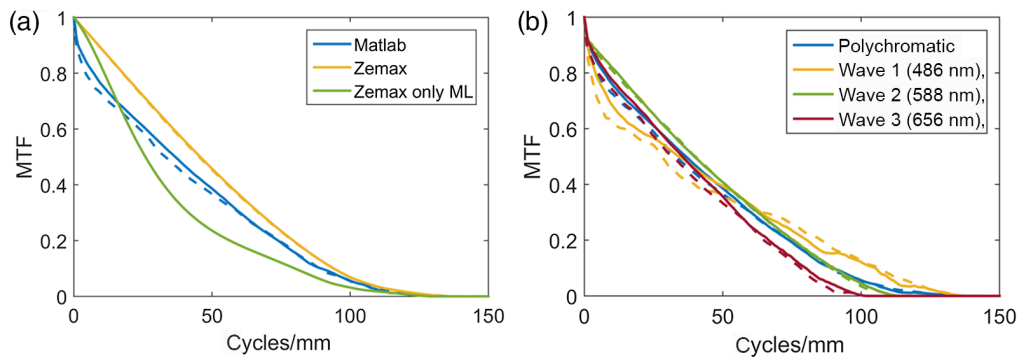


**Fig. 11** (a) Polychromatic MTF data for design 2 with a 4-mm aperture diameter from wave-optical simulation in Matlab<sup>®</sup> compared with the corresponding MTF from Zemax<sup>®</sup> without consideration of diffraction efficiency and (b) corresponding monochromatic wave-optical results. The dashed lines represent the respective sagittal MTFs.

MTF at low frequencies. This drop can be explained by stray light extending over considerable areas of the image plane due to light that is not diffracted in the desired direction and is in good agreement with considerations on hybrid systems in the literature.<sup>34</sup> The behavior of the MTF at the design wavelength (rounded: 588 nm) in Fig. 11(b) shows that this reduced diffraction efficiency is not mainly caused by wavelength dependency but must be dominated by effects of quantization.

## 5 Experimental Evaluation

### 5.1 Fabrication

For the experimental verification of the presented simulation results, the diffractive elements for both designs are fabricated as 8 phase level elements in fused silica at the Zentrum für Mikro- und Nanotechnologien at the Technische Universität Ilmenau. This is done using three subsequent lithography and reactive ion-etching steps. Three different chrome masks are used as masters with a mask-aligner for lithography. The masks are designed with a pixel size of 200 nm at a minimum feature size of about 3.1  $\mu\text{m}$ , to achieve a satisfactory geometric fidelity. The minimum feature size is also well above the minimum critical dimension of the applied processes of about 1  $\mu\text{m}$ . The ideal etch depth of the first step is calculated to be 640 nm, the second step is 320 nm, and the third step is 160 nm, giving a maximum depth of the structure of 1120 nm. Characterization of the fabricated structures using white light interferometry shows that this depth, which is critical for diffraction efficiency, is achieved quite precisely with a deviation from the ideal total depth at the measured parts of the diffractive elements below 7%. The maximum deviation, with a measured depth of about 1192 nm, shifts the design wavelength from 587.562 nm (*d*-line) to about 620 nm. Only a limited degradation of the polychromatic MTF is to be expected, according to wave-optical simulations depicted in Fig. 12.

### 5.2 Qualitative Evaluation via United States Air Force Test Chart and Broadband Illumination

As a first qualitative evaluation of the hybrid elements, imaging with broadband illumination and a color image sensor is performed. Therefore, the fabricated diffractive elements of the ALLs are mounted onto manual *x-y* adjustment stages using self-designed three-dimensional (3D)-printed adapters, which allow for placing the ALL elements directly behind each other, with a distance of zero [Fig. 13(a)]. To achieve the correct amount of relative shift between the phase plates and align the center of the shift with the optical axis, an additional adjustment setup is used, and a pre-designed alignment mark can be observed with a camera [Fig. 13(b)]. The adjusted ALL is then moved to the main setup for evaluation.

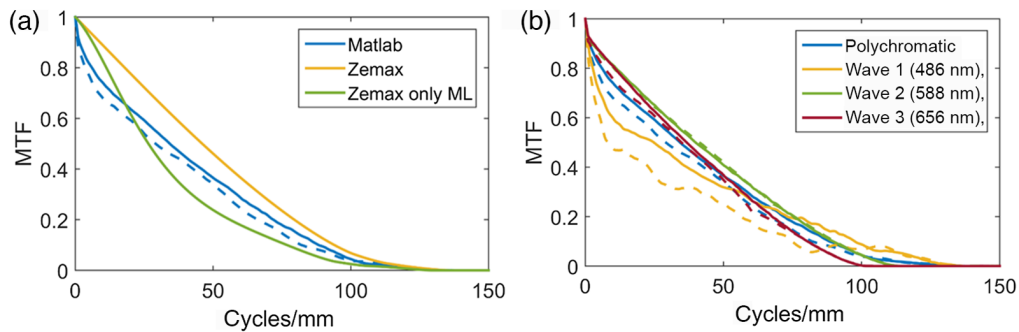


**Fig. 12** For comparison with Fig. 11: (a) polychromatic MTF data for design 2 with a 4-mm aperture diameter at a design wavelength of 620 nm from wave-optical simulation in Matlab®, compared with the corresponding MTF from Zemax® without consideration of diffraction efficiency and (b) corresponding monochromatic wave-optical results. The dashed lines represent the respective sagittal MTFs.

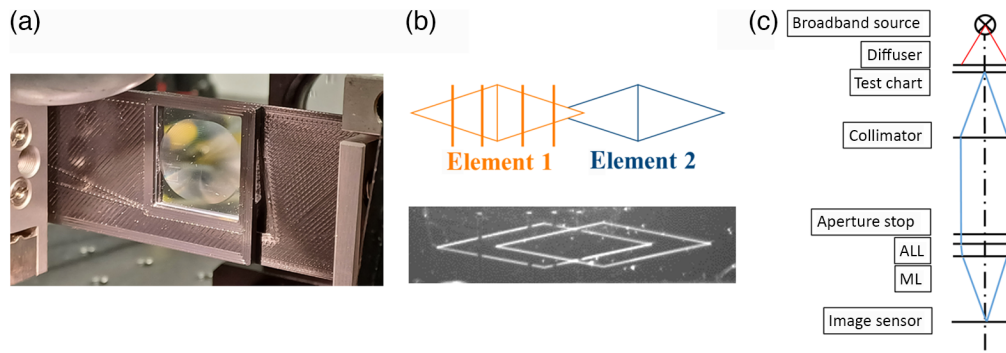
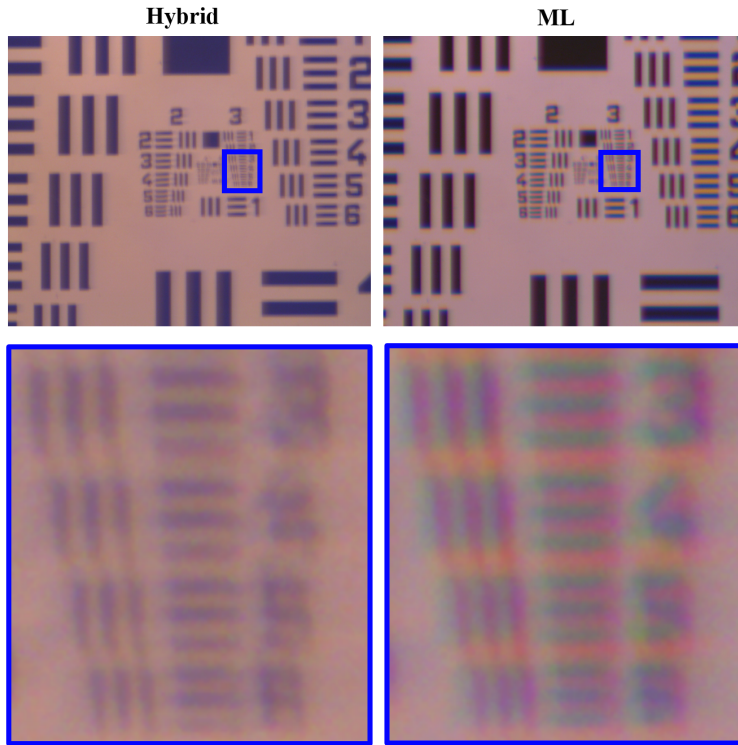


**Fig. 13** (a) ALL of design 1 within the 3D-printed adapter, (b) the principle of the adjustment mark, with an image taken in the adjustment setup: the triangular lines always intersect in the center between the shifted elements and the vertical lines mark the amount of shift for certain ML focal lengths; and (c) the schematic of the main test setup.

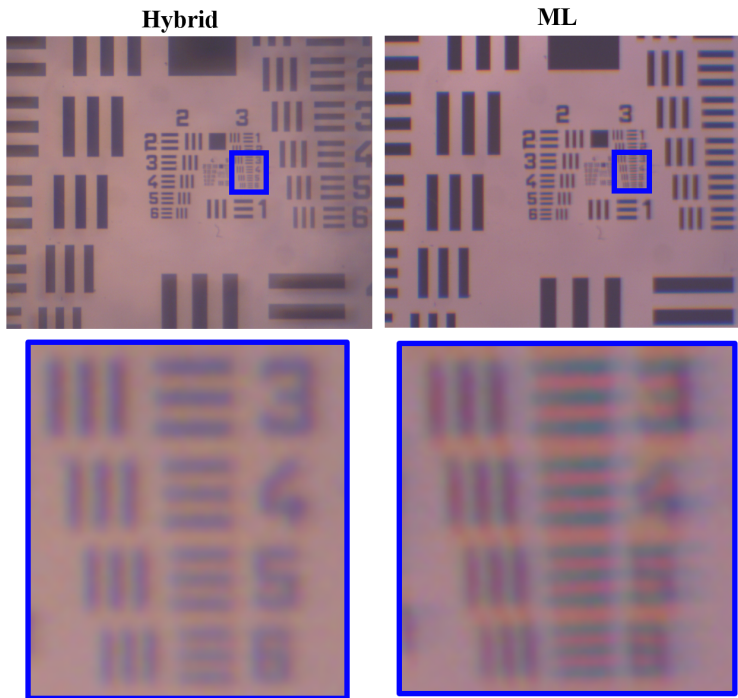
The main setup is as follows [Fig. 13(c)]: a United States Air Force (USAF) test chart is illuminated by a simple office lamp as the broadband source, imaged to infinity by a photographic lens (old Meopta Meoptar 4.5/210, 1938) as the collimator, and imaged back onto a color image sensor (UI-1240SE-C-HQ from IDS GmbH<sup>35</sup>) by the ML alone and the hybrid systems from designs 1 and 2, respectively. The optical axis is oriented vertically to reduce the effects of the gravity induced coma often observed with MLs.<sup>36,37</sup>

Figure 14 shows the resulting image for the hybrid element of design 1, at a focal length of the ML of 128 mm and an aperture diameter of 16 mm, compared with the ML alone with the same parameters. The color fringes in the image taken with the ML alone demonstrate that the correction of the axial color by the ALL works. These fringes are actually lateral color, caused by the distance between the aperture stop and the uncorrected ML. Apart from that, a drop in brightness can be noticed in the image taken with the hybrid element. This can be explained by the effect of the additional optical element without anti-reflection coating. Due to the automatic adaption of the exposure time, this can also at least partly explain the apparently reduced contrast of the structures imaged with the hybrid element. Because the measurements are not performed inside a clean room environment, dust particles, especially on the microstructured surfaces of the ALLs, are most certainly adding to this effect. The remaining part of contrast reduction can be explained by the drop of the MTF at low frequencies, due to diffraction efficiency, observed in the wave-optical simulations for design 2.

Figure 15 shows the results for design 2 at the same focal length of 128 mm and the aperture diameter of 6 mm. The same effects as for design 1 can be observed.



**Fig. 14** Comparison of color images taken with the hybrid element of design 1 and the ML alone at broadband illumination at a focal length of 128 mm and an aperture diameter of 16 mm. The magnified views show elements 3 to 6 of group 3 of the USAF resolution chart.



**Fig. 15** Comparison of color images taken with the hybrid element of design 2 and the ML alone at broadband illumination at a focal length of 128 mm and an aperture diameter of 6 mm. Due to the distance between aperture stop and the hybrid element, ghost images can be seen at higher field angles, where some rays only pass the ML without passing the ALL. The magnified views show elements 3 to 6 of group 3 of the USAF resolution chart.

### 5.3 MTF Measurement

To get quantitative experimental data, the experimental setup is adapted to use a fiber coupled supercontinuum white light (SC-) laser as illumination (SuperK Extreme from NKT Photonics<sup>38</sup>). The additional filter module SuperK Select (VIS-nIR)<sup>39</sup> allows for selecting different wavelength bands with about 10-nm bandwidths (full width at half maximum). Thereby the *F*-line, *d*-line, and *C*-line are used for illumination. A power meter is used to tune the three wavelength bands to about the same power. To improve the homogeneity of illumination despite the Gaussian beam profile, the collimated light from the fiber is expanded by a single positive lens [Fig. 16(c)]. To reduce the coherence, a rotating diffusing plate is placed as closely as possible behind the USAF test chart. Figures 16(a) and 16(b) show how the rotation of the diffuser reduces the speckle contrast. The remaining setup is the same as for the qualitative measurements, apart from the image sensor: now a monochromatic sensor with 1.67- $\mu\text{m}$  pixel size and 8 bit intensity resolution is used (UI-1492LE-M from IDS GmbH<sup>40</sup>).

To determine the MTF from the images, the well-known slanted edge method is applied: the edge spread function (ESF) of the optical system is measured by analyzing the image of an edge of the pattern. From the ESF, the line spread function (LSF) is calculated via differentiation. The LSF can be regarded as a one-dimensional PSF, and the tangential and sagittal MTFs are calculated via Fourier transformation from two perpendicular LSFs.<sup>33</sup> Using an edge that is slightly tilted with regard to the sensor pixel grid, subpixel sampling of the ESF can be achieved by modeling the edge and projecting the intensities of multiple pixel rows onto a new coordinate that is perpendicular to the slanted edge.<sup>41</sup>

The images taken with the ML, tuned to a focal length of 64 mm and a stop diameter of 16 mm, for design 1 and the ML alone are shown in Fig. 17. The regions of interest (ROIs) used for evaluation are selected to be close to the optical axis and are marked with red

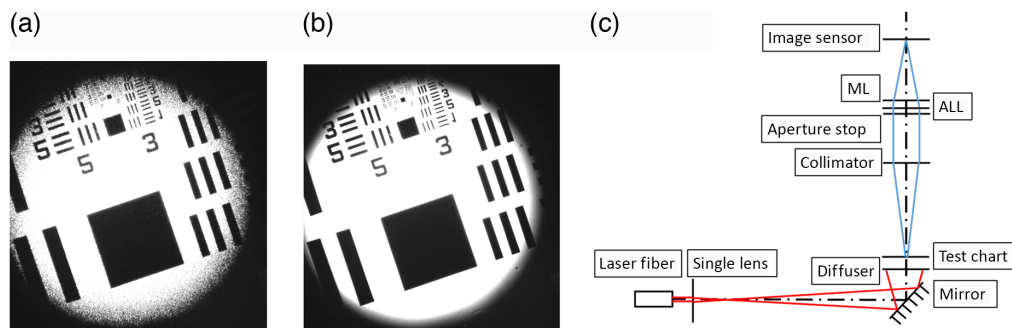


**Fig. 16** (a) Comparison of an image with stationary diffuser with clearly visible speckles and (b) with rotating diffuser with low speckle contrast, with the circular, slightly blurred limitation of the illuminated field being caused by the quite small aperture of the mount of the rotating diffuser and (c) experimental setup.

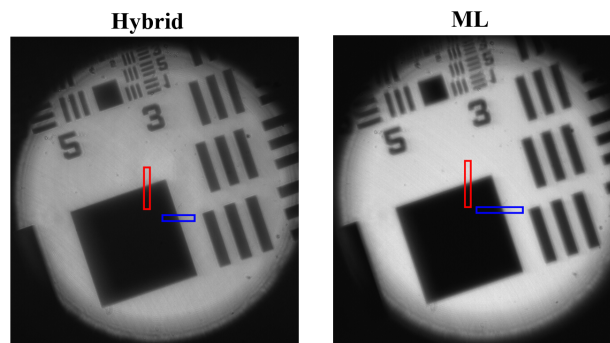


**Fig. 17** Images for a ML focal length of 64 mm and an aperture diameter of 16 mm for the hybrid element of design 1 and the ML alone. The red rectangle marks the ROI for determination of the tangential MTF, and the blue rectangle marks the ROI for the sagittal MTF.

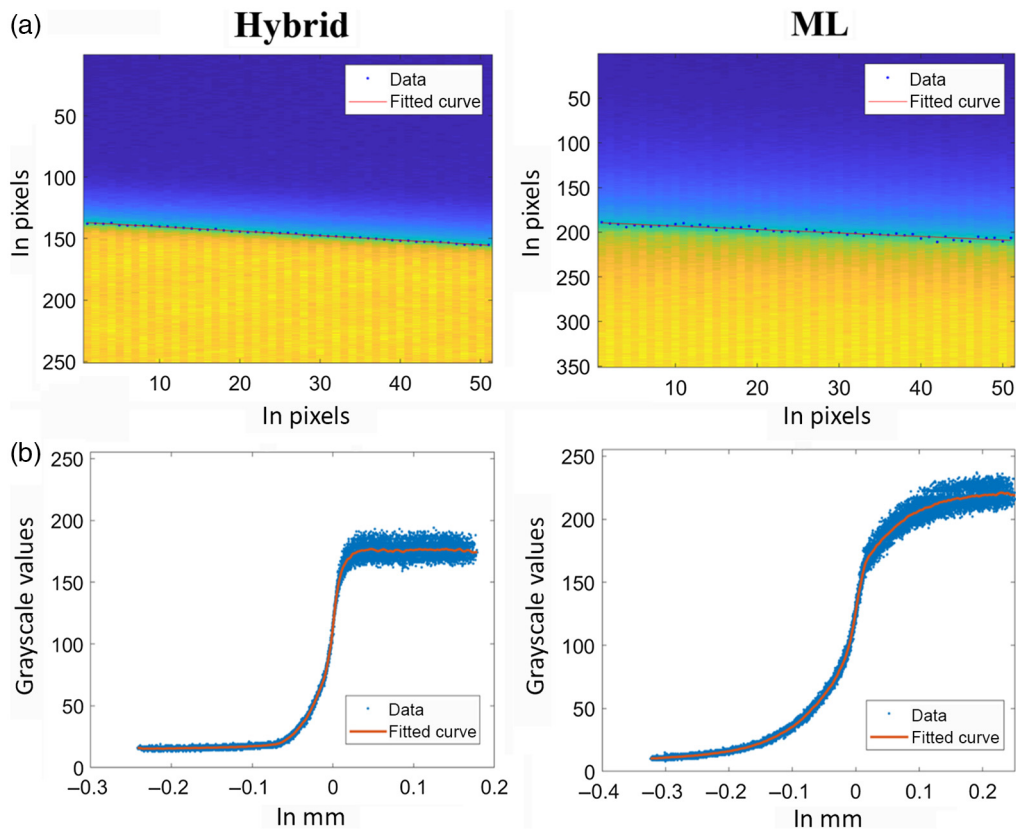


**Fig. 18** (a) Modeling of the edge position and (b) fit of the ESF to the projected intensity data, for a focal length of the ML of 64 mm and an aperture diameter of 16 mm for both the hybrid element of design 1 and the ML alone.

(tangential) and blue (sagittal) rectangles. Here, the sagittal and tangential directions are defined by the coordinates from the designs, with the  $x$ -coordinate (direction of the ALL element shift) along the sagittal direction.

Figure 18(a) shows the modeling of the tangential edge position for the ROIs from Fig. 17. In Fig. 18(b), the projected intensity data, as well as the ESF fitted in Matlab<sup>®</sup> as a smoothing spline, are shown. This fitted ESF is then used to determine the LSF and the MTF.

The resulting MTF data are compared with the corresponding Zemax data in Figs. 19(a). Figure 19(b) shows the same comparison for a ML focal length of 128 mm.

The first important point to note is that the measured MTF for the ML alone matches the simulated MTF from Zemax<sup>®</sup> quite well. This confirms the validity of the measured data. For both focal lengths, either the tangential or the sagittal MTF of the hybrid element exceeds the data from the ML alone over a certain frequency range. The measured performance at a focal length of 64 mm is superior to the performance at 128 mm. At 128 mm, the relevant improvement is limited to frequencies below 35 cycles/mm, in which both the MTF of the ML and the tangential MTF of the hybrid element approach zero, indicating contrast reversal at higher frequencies. Similar to the wave-optical simulation for design 2, the improvement at a focal length of 64 mm seems to be most pronounced for medium frequencies. At the same time the difference between the ideal MTF from Zemax<sup>®</sup> and the measured MTF is larger than that expected from the wave-optical simulations. In addition to the effects of dust particles, a possible reason for this is misalignment of the ALLs. The ray-tracing-based simulation shows that a decenter of merely 0.016 mm in the  $y$ -direction or a tilt of 0.65 deg around the optical axis of the first ALL element is enough to cause the tangential MTF to approach zero before 40 cycles/mm, similar to the behavior observed in Fig. 19(b). Corresponding MTF curves for these cases are shown in Appendix D. Both values are highly plausible due to the simple visual adjustment of the element positions (for orientation: the vertical lines of the adjustment mark

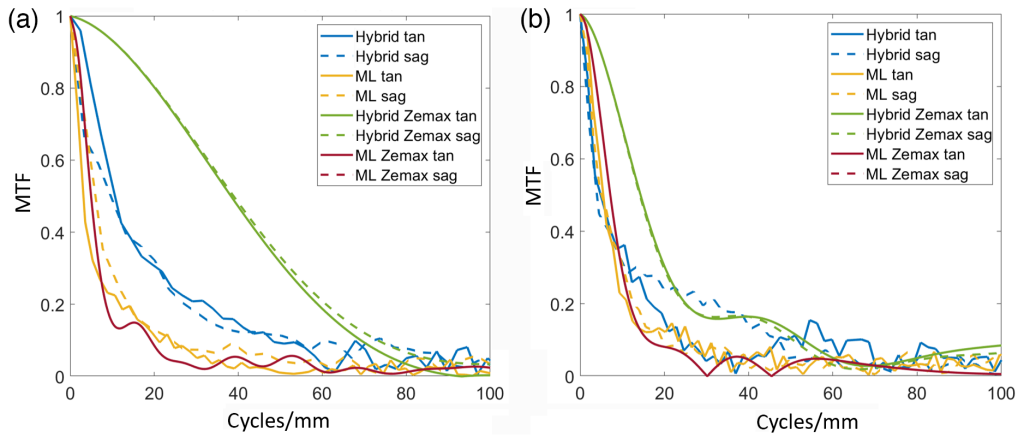


**Fig. 19** Comparison of measured MTF data and corresponding Zemax<sup>®</sup> data for the hybrid element of design 1 and the ML alone (aperture diameter 16 mm), at a ML focal length of (a) 64 mm and (b) 128 mm.

depicted in Fig. 13(b) have a width of 0.1 mm). Additionally, the MTF is probably more sensitive to diffraction efficiency due to the steeper wavefronts at an aperture of 16 mm than at the simulated 4 mm.

The MTF results for design 2 are shown in Fig. 20.

For both focal lengths of design 2, there is no significant difference between the MTF curves for the hybrid element and the ML alone. At the same time, both curves seem to match the expected MTF for the ML alone from Zemax<sup>®</sup> quite well. For the 64 mm focal length, it has to be noted that the depicted MTF curve from Zemax<sup>®</sup> for the ML alone was not found by optimizing the distance between the ML and image plane for the minimum spot diameter, but it was found by manually adjusting this distance, resulting in an improved MTF. Because here the aperture diameter of 6 mm is quite close to the wave-optically simulated aperture diameter of 4 mm, the most plausible explanation for the lack of improvement of the MTF by the hybrid element is the imperfect adjustment of the ALL elements within the experimental setup. Ray-tracing-based simulations show that shift errors  $\Delta d$  of -0.1 mm for a ML focal length of 64 mm and -0.07 mm for a ML focal length of 128 mm lead to similar MTF curves for design 2, as observed in Fig. 20. At the same time, design 2 appears to be far less sensitive to the decenter of one ALL element in the  $y$ -direction than design 1. A decenter in the  $y$ -direction of 0.15 mm is necessary to cause a similar degradation of the MTF as the shift errors. The MTF curves for the described shift errors are shown in Appendix D.

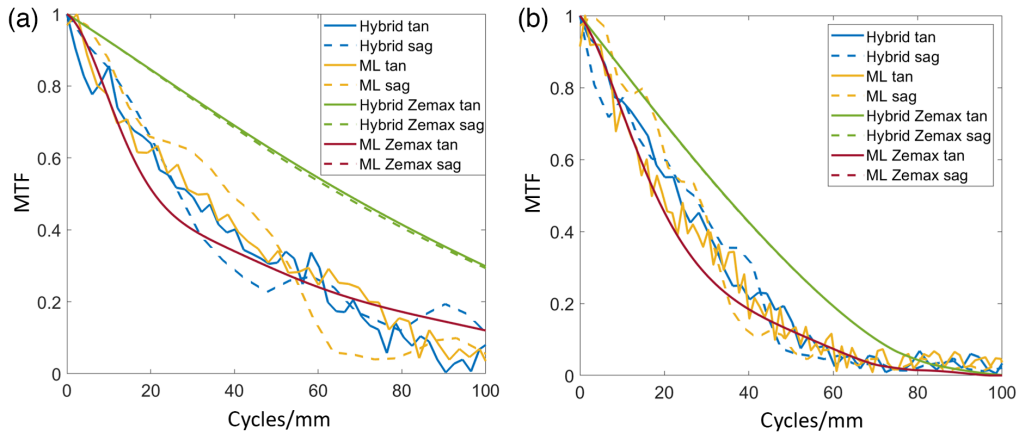


**Fig. 20** Comparison of measured MTF data and corresponding Zemax<sup>®</sup> data for the hybrid element of design 2 and the ML alone (aperture diameter 6 mm) at a ML focal length of (a) 64 mm and (b) 128 mm.

## 6 Conclusions

For optical systems based on tunable MLs and used with a broad wavelength range, it is desirable to create lens modules with a performance similar to achromats over the whole tuning range. To this end, we have demonstrated that the application of diffractive ALLs for the reduction of the axial color and spherical aberration of MLs over the whole tuning range is promising. The most important advantages over the combination of multiple MLs for refractive tunable achromats are smaller installation space and larger tuning range of the corrected element. Although suffering from typical shortcomings of diffractive elements in broadband applications, wave-optical simulations and experimental data demonstrate the overall improvement of the image quality by the diffractive ALLs. The comparably small improvements found in the measured polychromatic MTF can be explained by imperfect adjustments of the ALLs within the experimental setup. At the same time even without a large improvement of the polychromatic MTF, the reduction of the differences in image quality and focus position for different wavelengths can largely improve the visual impression, e.g., in photographic color imaging. Further experimental evaluation, ideally within a clean room environment, with improved procedures and setups for adjustment of the ALL elements, as well as the design of optical systems based on the hybrid tunable elements, seem promising.

## 7 Appendix A

For DOEs optimized for the first diffraction order, the period of the diffractive structures is the distance over which the phase function for the design wavelength increases by  $2\pi$ . Depending on the number of phase levels used for quantization, this defines the minimum feature size that has to be fabricated.

The equations for the phase functions of an ALL tuned by translation is shown in Table 1. The gradient of the phase function is given by the first derivative. Equations (4) and (5) are the first derivative of the phase functions for the basic parabolic ALL in the  $x$ - and  $y$ - directions, respectively:

$$\frac{\delta\Phi_{\text{trans},1}}{\delta x} = A(x^2 + y^2), \quad (4)$$

$$\frac{\delta\Phi_{\text{trans},1}}{\delta y} = Axy. \quad (5)$$

Figure 21 shows the geometry of a translational ALL element clipped to the size required for a circular aperture. It is clear that in this case the maximum gradient, and with it the minimum period of the diffractive structures, is reached at the maximum  $x$ -coordinate.

The higher polynomial terms should not change the fundamental character of the phase function as a radial symmetric function with an additional gradient in the  $x$ -direction for tuning. Therefore, it can be assumed that for the non-parabolic ALLs, the gradient in the  $x$ -direction will still be the critical one.

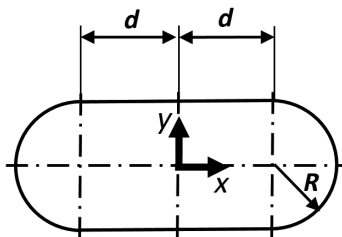


**Fig. 21** Geometry of one element of a translational ALL clipped to the necessary size for a circular aperture with radius  $R$  and a maximum amount of shift  $d$ .

For the case of the translational basic parabolic ALL, the local period of the diffractive structures is calculated from

$$\frac{2\pi}{\frac{\delta\Phi_{\text{trans},1}}{\delta x}} = \frac{2\pi}{A(x^2 + y^2)}. \quad (6)$$

Inserting the coordinates of the maximum gradient  $x = R + d$  and  $y = 0$  yields the minimum period of the diffractive structures, as shown in Table 1.

The equations for the phase functions of the elements for a diffractive ALL tuned by rotation are also included in Table 1. As shown by Bernet and Ritsch-Marte in Ref. 14, the strongest gradient occurs in the radial direction, and the corresponding first derivative yields

$$\frac{\delta\Phi_{\text{rot},1}}{\delta r} = 2Ar\varphi. \quad (7)$$

The angle coordinate  $\varphi$  runs from  $-\pi$  to  $\pi$ , and the maximum radial coordinate  $r$  is given by  $R$ .<sup>14</sup> The minimum period of the diffractive structures for the basic parabolic ALL tuned by rotation results in

$$\frac{2\pi}{\frac{\delta\Phi_{\text{rot},1}}{\delta r}} = \frac{2\pi}{2AR\pi} = \frac{1}{AR}. \quad (8)$$

## 8 Appendix B

Tables 5, 6, and 7 provide the full system description of design 1.

**Table 5** Surface data for design 1, S, spherical surface; Binary 1, binary 1 surface type from Zemax<sup>®</sup> for the diffractive surfaces; M, membrane; and (E), thickness measured at the edge of the surface instead of the optical axis. The description for the binary 1 surfaces is shown in Table 7.

No.	Type	Radius (mm)	Thickness (mm)	Clear semi diameter (mm)	Material
1	Vignetting stop	Inf	0.000	8.000	
2	S	Inf	1.000	9.500	Fused silica
3	Binary 1	Inf	0.000	9.500	
4	Binary 1	Inf	1.000	9.500	Fused silica
5	S	Inf	0.000	9.500	
6	Vignetting stop	Inf	2.000	8.000	
7	S	Inf	0.470	10.000	
8	S	Inf	1.000	10.000	BK7
9	S	Inf	4.175 (E)	10.000	
10	M, stop	Table 6	Table 6	10.000	OL1129_VIS_NIR
11	S	Inf	0.500	10.000	BK7
12	S	Inf	Table 6	10.000	
13	S	Inf	Table 6	10.000	
14	IMA	Inf			

**Table 6** Values for the surface data that vary between the different configurations for design 1 and (E), thickness measured at the edge of the surface instead of the optical axis.

Surface No.	Focal length ML in mm			
	64	128	-103	-51
	Radii of membrane in mm			
10	24.478	48.780	-39.216	-19.677
	Thicknesses in mm			
10	2.383 (E)	2.785 (E)	3.687 (E)	4.187 (E)
12	4.672	4.270	3.368	2.868
13	51.162	115.477	-103.447	-50.462

**Table 7** Coefficients for the first Zemax® binary 1 surfaces in design 1. The coefficients for the second binary 1 surface are the same with the opposite sign. The phase function is the sum of the polynomial terms multiplied by their respective coefficients. The coefficients are dimensionless, because the  $x$  and  $y$  coordinate values are divided by a norm radius of 1 mm before calculating the polynomial terms.

Term	Coefficient	Term	Coefficient	Term	Coefficient
$x^1y^0$	$4.420e^{-5}$	$x^4y^0$	$-1.034e^{-7}$	$x^1y^4$	$-0.013$
$x^0y^1$	0.000	$x^3y^1$	0.000	$x^0y^5$	0.000
$x^2y^0$	$4.816e^{-6}$	$x^2y^2$	$-1.934e^{-7}$	$x^6y^0$	$6.910e^{-10}$
$x^1y^1$	0.000	$x^1y^3$	0.000	$x^5y^1$	0.000
$x^0y^2$	$4.102e^{-7}$	$x^0y^4$	$-2.920e^{-4}$	$x^4y^2$	$1.822e^{-09}$
$x^3y^0$	1.308	$x^5y^0$	$-2.509e^{-3}$	$x^3y^3$	0.000
$x^2y^1$	0.000	$x^4y^1$	0.000	$x^2y^4$	$1.964e^{-9}$
$x^1y^2$	3.901	$x^3y^2$	$-8.366e^{-3}$	$x^1y^5$	0.000
$x^0y^3$	0.000	$x^2y^3$	0.000	$x^0y^6$	$7.589e^{-5}$

## 9 Appendix C

Tables 8, 9, and 10 provide the full system description of design 2.

**Table 8** Surface data for design 2; S, spherical surface; Binary 1, binary 1 surface type from Zemax® for the diffractive surfaces; M, membrane; and (E), thickness measured at the edge of the surface instead of the optical axis. The description for the binary 1 surfaces is shown in Table 10.

No.	Type	Radius (mm)	Thickness (mm)	Clear semi diameter (mm)	Material
1	S	Inf	0.470	10.000	BK7
2	S	Inf	4.175 (E)	10.000	
3	M, stop	Table 9	Table 9	10.000	OL1129_VIS_NIR
4	S	Inf	0.500	10.000	BK7
5	S	Inf	Table 9	10.000	
6	S	Inf	2.000	10.000	
7	Vignetting stop	Inf	0.000	3.000	
8	S	Inf	1.000	4.500	Fused silica
9	Binary 1	Inf	0	4.500	
10	Binary 1	Inf	1.000	4.500	Fused silica
11	S	Inf	0.000	4.500	
12	Vignetting stop	Inf	Table 9	3.000	
14	IMA	Inf			

**Table 9** Values for the surface data that vary between the different configurations for design 2 and (E), thickness measured at the edge of the surface instead of the optical axis.

Surface No.	Focal length ML in mm			
	64	128	-103	-51
	Radii of membrane in mm			
3	24.478	48.780	-39.216	-19.677
	Thicknesses in mm			
3	2.383 (E)	2.785 (E)	3.687 (E)	4.187 (E)
5	4.672	4.270	3.368	2.868
12	48.952	110.252	-105.914	-56.092

**Table 10** Coefficients for the first Zemax® binary 1 surfaces in design 2. The coefficients for the second binary 1 surface are the same with opposite sign. The phase function is the sum of the polynomial terms multiplied by their respective coefficients. The coefficients are dimensionless, because the  $x$  and  $y$  coordinate values are divided by a norm radius of 1 mm before calculating the polynomial terms.

Term	Coefficient	Term	Coefficient	Term	Coefficient
$x^1y^0$	$-2.223e^{-7}$	$x^4y^0$	$1.513e^{-12}$	$x^1y^4$	$-8.063e^{-3}$
$x^0y^1$	0.000	$x^3y^1$	0.000	$x^0y^5$	0.000
$x^2y^0$	$4.748e^{-11}$	$x^2y^2$	$1.141e^{-11}$	$x^6y^0$	$-2.065e^{-14}$
$x^1y^1$	0.000	$x^1y^3$	0.000	$x^5y^1$	0.000
$x^0y^2$	-0.053	$x^0y^4$	$-3.698e^{-3}$	$x^4y^2$	$-1.597e^{-13}$
$x^3y^0$	0.752	$x^5y^0$	$-1.632e^{-3}$	$x^3y^3$	0.000
$x^2y^1$	0.000	$x^4y^1$	0.000	$x^2y^4$	$-7.279e^{-13}$
$x^1y^2$	2.245	$x^3y^2$	$-5.502e^{-3}$	$x^1y^5$	0.000
$x^0y^3$	0.000	$x^2y^3$	0.000	$x^0y^6$	$3.401e^{-9}$

### 10 Appendix D

Figures 22 and 23 provide an estimate of the sensitivity to ALL alignment for design 1 and design 2 based on MTF data from ray-tracing simulations.

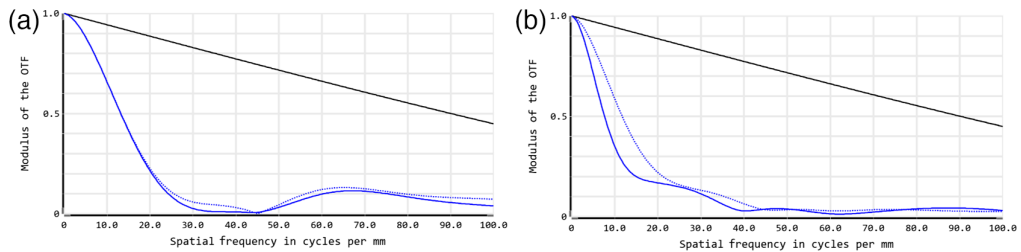


**Fig. 22** Ray-tracing based MTF curves from Zemax® for design 1 at a focal length of 128 mm (a) with a decenter of the first ALL element in the  $y$ -direction of 0.016 mm and (b) with a tilt of the first ALL element around the  $z$ -axis (=optical axis) of 0.65 deg. The dashed line represents the corresponding sagittal MTF.

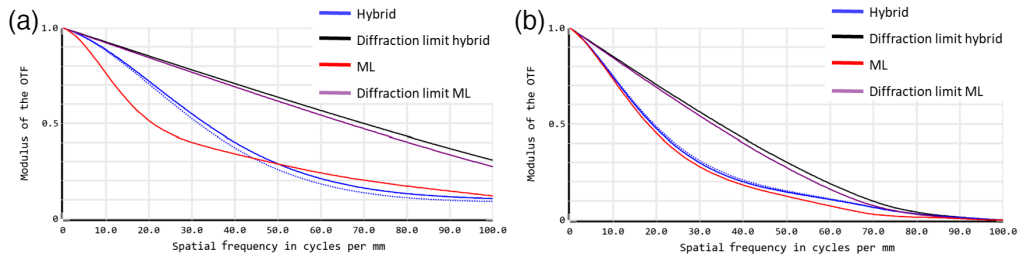


**Fig. 23** Ray-tracing based MTF curves from Zemax® for design 2 (blue) compared with the ML alone (red), (a) at a ML focal length of 64 mm with a shift error  $\Delta d$  of  $-0.1$  mm and (b) at a ML focal length of 128 mm with a shift error  $\Delta d$  of  $-0.07$  mm. The dashed line represents the sagittal MTF. The difference between the diffraction limits for the hybrid element and the ML is caused by the slightly larger numerical aperture (NA) of the hybrid element due to its slightly shorter focal length at the same ML focal length.

## Acknowledgments

The authors would like to give special thanks to Patrick Fesser and the staff of the Zentrum für Mikro- und Nanotechnologien at the Technische Universität Ilmenau for performing the fabrication of the diffractive elements. Parts of the work presented in this paper were funded by the Deutsche Forschungsgemeinschaft (DFG) (Grant No. 390737909) “Wavesynth.” Open Access is enabled and organized by SPIE’s “Read and Publish” agreement with the German National Library of Science and Technology. The authors declare no competing interests.

## References

1. H. Ren and S.-T. Wu, *Introduction to Adaptive Lenses*, John Wiley & Sons, Inc., Hoboken, New Jersey (2012).
2. S. Sinzinger, “Diffractive and refractive microoptics,” in *Comprehensive Microsystems*, Y. B. Gianchandani, O. Tabata, and H. Zappe, Eds., Elsevier, Oxford (2007).
3. H. Zappe and C. Duppé, *Tunable Micro-Optics*, Cambridge University Press, Cambridge UK (2015).
4. Holochip Corporation, “Variable focus lenses,” <https://www.holochip.com/photonics> (accessed 02 Nov. 2021).
5. Optotune Switzerland AG, “Focus tunable lenses,” <https://www.optotune.com/focus-tunable-lenses> (accessed 02 Nov. 2021).
6. P. Zhao, Ç. Ataman, and H. Zappe, “Gravity-immune liquid-filled tunable lens with reduced spherical aberration,” *Appl. Opt.* **55**, 7816–7823 (2016).
7. K. Mishra et al., “Optofluidic lens with tunable focal length and asphericity,” *Sci. Rep.* **4**, 6378 (2014).
8. Corning Incorporated, “Corning varioptic lenses,” <https://www.corning.com/emea/de/innovation/corning-emerging-innovations/corning-varioptic-lenses/variable-focus-lenses-a-series.html> (accessed 02 Nov. 2021).
9. F. Santiago et al., “Large aperture adaptive doublet polymer lens for imaging applications,” *J. Opt. Soc. Am. A* **31**, 1842–1846 (2014).
10. F. C. Wippermann et al., “Mechanically assisted liquid lens zoom system for mobile phone cameras,” *Proc. SPIE* **6289**, 62890T (2006).
11. L. Lenk, B. Mitschunas, and S. Sinzinger, “Design method for zoom systems based on tunable lenses,” *Opt. Eng.* **61**(6), 065103 (2022).
12. L. W. Alvarez, “Two-element variable-power spherical lens,” U.S. Patent 3,305,294 (1967).
13. A. W. Lohmann, “A new class of varifocal lenses,” *Appl. Opt.* **9**, 1669–1671 (1970).
14. S. Bernet and M. Ritsch-Marte, “Adjustable refractive power from diffractive moiré elements,” *Appl. Opt.* **47**, 3722–3730 (2008).
15. S. Bernet, W. Harm, and M. Ritsch-Marte, “Demonstration of focus-tunable diffractive Moiré-lenses,” *Opt. Express* **21**, 6955–6966 (2013).
16. S. Bernet and M. Ritsch-Marte, “Multi-color operation of tunable diffractive lenses,” *Opt. Express* **25**, 2469–2480 (2017).
17. N. Bregenzer et al., “Demonstration of a multi-color diffractive lens with adjustable focal length,” *Opt. Express* **28**, 30150–30163 (2020).
18. A. Grewe, P. Fesser, and S. Sinzinger, “Diffractive array optics tuned by rotation,” *Appl. Opt.* **56**, A89–A96 (2017).
19. A. Bielke, C. Pruss, and W. Osten, “Design of a variable diffractive zoom lens for interferometric purposes,” *Opt. Eng.* **56**(1), 014104 (2017).
20. A. Grewe, M. Hillenbrand, and S. Sinzinger, “Aberration analysis of optimized Alvarez–Lohmann lenses,” *Appl. Opt.* **53**, 7498–7506 (2014).
21. A. Grewe et al., “Advanced phase plates for confocal hyperspectral imaging systems,” in *Imaging and Appl. Opt., OSA Tech. Digest*, Optica Publishing Group, p. AW1B.2 (2013).
22. P. Valley et al., “Adjustable hybrid diffractive/refractive achromatic lens,” *Opt. Express* **19**, 7468–7479 (2011).
23. W. Harm et al., “Dispersion tuning with a varifocal diffractive-refractive hybrid lens,” *Opt. Express* **22**, 5260–5269 (2014).

24. L. Lenk and S. Sinzinger, "Diffractive Alvarez-Lohmann lenses for aberration correction: towards hybrid tunable achromats," Paper presented at *ICO-25/OWLS-16 2022*, Dresden (2022).
25. Y. Zou et al., "Miniature tunable multi-element Alvarez lenses," in *Int. Conf. Opt. MEMS and Nanophotonics*, pp. 23–24 (2014).
26. B. C. Kress and P. Meyrueis, *Applied Digital Optics*, John Wiley & Sons, Ltd, Chichester (2009).
27. Optotune Switzerland AG, "ML-20-37-lens," <https://www.optotune.com/ml-20-37-lens> (accessed 02.Nov. 2021).
28. M. J. Kidger, *Fundamental Optical Design*, SPIE Press, Bellingham, Washington (2001).
29. S. F. Busch et al., "Extending the Alvarez-lens concept to arbitrary optical devices: tunable gratings, lenses, and spiral phase plates," *IEEE Trans. Terahertz Sci. Technol.* **7**(3), 320–325 (2017).
30. S. Sinzinger and J. Jahns, *Microoptics*, 2nd ed., Wiley-VCH, Weinheim (2003).
31. M. Nicholson, "How to model a black-box optical system using Zernike coefficients," Zemax Knowledgebase, 2021, <https://support.zemax.com/hc/en-us/articles/1500005575422-How-to-model-a-black-box-optical-system-using-Zernike-coefficients>.
32. K. Matsushima, "Shifted angular spectrum method for off-axis numerical propagation," *Opt. Express* **18**, 18453–18463 (2010).
33. B. Dörband, H. Müller, and H. Gross, *Metrology of Optical Components and Systems*, Handbook of Optical Systems, Vol. **5**, Wiley-VCH, Weinheim (2008).
34. C. Londoño and P. P. Clark, "Modeling diffraction efficiency effects when designing hybrid diffractive lens systems," *Appl. Opt.* **31**, 2248–2252 (1992).
35. IDS GmbH, "UI-1240SE-C-HQ," <https://de.ids-imaging.com/store/ui-1240se.html> (accessed 19 Aug. 2022).
36. M. Quintavalla et al., "Optical characterization and adaptive optics correction of polymer adaptive lens aberrations," *Appl. Opt.* **58**, 158–163 (2019).
37. J. M. Marín et al., "Optical characterization of electro-optics lenses for researching in optics," *Proc. SPIE* **11488**, 114880P (2020).
38. NKT Photonics A/S, "SuperK extreme product guide," <https://www.nktphotonics.com/product-manuals-and-documentation/> (accessed 19.Aug. 2022).
39. NKT Photonics A/S, "SuperK select," <https://www.nktphotonics.com/products/super-continuum-white-light-lasers/superk-select/> (accessed 19 Aug. 2022).
40. IDS GmbH, "UI-1492LE-M," <https://de.ids-imaging.com/store/ui-1492le.html> (accessed 19 Aug. 2022).
41. F. Viallefont-Robinet et al., "Comparison of MTF measurements using edge method: towards reference data set," *Opt. Express* **26**, 33625–33648 (2018).

**Leonhard Lenk** received his BS and MS degrees in mechanical engineering in 2016 and 2018, respectively. He has been a PhD student at the optical engineering group of the Technische Universität Ilmenau, Germany, since 2018. His research interests include optical system design and refractive and diffractive tunable lenses.

**Stefan Sinzinger** received his PhD from the Friedrich-Alexander Universität Erlangen-Nürnberg in 1993 and the Habilitation from the Fernuniversität Hagen in 2001. Currently, he is a professor for technische optik (optical engineering) at the Technische Universität Ilmenau, Germany. He was a coauthor of the textbook *Microoptics*, and his research interests include design and fabrication of microoptical elements as well as microoptical systems integration.